

The Allen Cell Structure Segmente: a new open source toolkit for segmenting 3D intracellular structures in fluorescence microscopy images

Jianxu Chen, Liya Ding, Matheus P. Viana, Melissa C. Hendershott, Ruian Yang, Irina A. Mueller, and Susanne M. Rafelski

Abstract

A continuing challenge in quantitative cell biology is the accurate and robust 3D segmentation of structures of interest from fluorescence microscopy images in an automated, reproducible, and widely accessible manner for subsequent interpretable data analysis. We describe the Allen Cell Structure Segmente, a new Python-based open source toolkit developed for 3D segmentation of intracellular structures in fluorescence microscope images. This toolkit brings together classic image segmentation and iterative deep learning workflows first to generate initial high-quality 3D intracellular structure segmentations and then to easily curate these results to generate the ground truths for building robust and accurate deep learning models. The toolkit takes advantage of the high-replicate 3D live cell image data collected at the Allen Institute for Cell Science of over 30 endogenous fluorescently tagged human induced pluripotent stem cell (hiPSC) lines. Each cell line represents a different intracellular structure with one or more distinct localization patterns within undifferentiated hiPS cells and hiPSC-derived cardiomyocytes. The Allen Cell Structure Segmente consists of two complementary elements, a classic image segmentation workflow with a restricted set of algorithms and parameters and an iterative deep learning segmentation workflow. We created a collection of 20 classic image segmentation workflows based on 20 distinct and representative intracellular structure localization patterns as a “lookup table” reference and starting point for users. The iterative deep learning workflow can take over when the classic segmentation workflow is insufficient. Two straightforward “human-in-the-loop” curation strategies convert a set of classic image segmentation workflow results into a set of 3D ground truth images for iterative model training without the need for manual painting in 3D. The deep learning model architectures used in this toolkit were designed and tested specifically for 3D fluorescence microscope images and implemented as readable scripts. This toolkit was applied to the robust segmentation of fluorescent lamin B1, which exhibits significant variability in its localization pattern during the cell cycle. The Allen Cell Structure Segmente thus leverages state of the art computer vision algorithms in an accessible way to facilitate their application by the experimental biology researcher.

Introduction

Modern fluorescence microscopy has revolutionized imaging of tissues, cells, subcellular structures, and proteins [Kervrann et al., 2016]. The resulting multi-dimensional image data (3D, time-lapse, multiple imaging channels, or combinations thereof, etc.) require further analysis with a variety of qualitative and quantitative approaches. Simple visual inspection of small image data sets is used to rapidly assess general image quality or compare differences among experimental conditions. Quantitative and automated analysis approaches, however, become necessary when the number of images is large, the differences between experimental conditions are subtle or complex, or the image data and their interpretations are used to develop data-driven analyses and models. Quantifying images becomes especially important when dealing with 3D image data where even a straightforward comparison between two conditions can be difficult without quantitative measurements. Segmentation, the identification of every pixel (or voxel) that is either part or not part of that object, is key to extracting interpretable, quantitative measurements of an object in an image, permitting measurement of size, shape, number of objects and intensity of a given object, for example.

The large number of different sizes and shapes of structures found in cells makes image segmentation particularly challenging. Furthermore, 3D image data are inherently harder to work with than 2D images, presenting an additional challenge for cellular image segmentation and analysis. Existing 3D image segmentation methods can be categorized as classic image processing algorithms, traditional machine learning, and deep learning methods. Classic image processing algorithms are the most widely used by the cell biological research community and are accessible in two main ways. Some algorithms are available as collections of basic functions in several open platforms, including the widely-used ImageJ [Schindelin et al., 2012], CellProfiler [Carpenter et al., 2006, McQuin et al., 2018], Icy [De Chaumont et al., 2012], and ITK-SNAP [Yushkevich et al., 2006]. However, basic functions in the open platforms are often not sufficiently accurate or up to date [Jerman et al., 2016]. Other published algorithms may be designed for a specific structure in a specific imaging modality and are often implemented and released individually [Neila et al., 2016, Hodneland et al., 2013, Smith and Barton, 2014]. Compared to general image processing platforms, such tools are less broadly applicable and often less convenient to apply.

Machine learning algorithms can also facilitate segmentation of 2D and 3D fluorescence microscopy images. Traditional machine learning algorithms, e.g., random forest and supporting vector machine, have been integrated successfully into openly accessible tools such as trainable WEKA segmentation [Arganda-Carreras et al., 2017] in ImageJ and ilastik [Sommer et al., 2011]. Users simply manually paint on selective pixels/voxels as foreground and background samples to create a ground truth training set. A traditional machine learning model is then automatically trained and applied on all selected images. While easy to use, these traditional machine learning models and tools are less effective than deep learning models especially when segmenting objects with occluded boundaries (e.g. tightly packed or highly textured objects [Çiçek et al., 2016, Chen et al., 2016B, Chen et al., 2017]). Unfortunately, deep learning models are “training data hungry.” Thus tedious manual painting in 3D quickly becomes prohibitive for generating sufficient 3D ground truth data. Additionally, even if an adequate 3D ground truth can be prepared, access to convenient tools for building/deploying these deep learning models is currently prohibitive for many biologists. Existing tools, such as NiftyNet [Gibson et al., 2018] or DLTK [Pawlowski et al., 2017], are difficult to use without sufficient experience in deep learning and computer vision. Other tools, e.g., Aivia Cloud [DRVISION, 2018], are easier to use but not openly accessible.

The Allen Institute for Cell Science has developed a pipeline that generates high-replicate, dynamic image data on cell organization and activities using a collection of endogenous fluorescently tagged human induced pluripotent stem cell (hiPSC) lines (Allen Cell Collection; allencell.org; [Roberts et al.,

2017]). Most lines express a monoallelic mEGFP-tagged protein that represents a particular intracellular structure (exceptions are the tagged sialyltransferase 1 line and the Ras-related protein Rab5-a line, which are also available as biallelic lines and the centrin-2 line, which is tagged with mTagRFP-T). To enable quantitative image and data analyses, we generated accurate and robust segmentations for over 30 intracellular 3D structure localization patterns. By developing and testing a diverse set of traditional segmentation algorithms on a wide range of intracellular structures, we identified a conceptually simple “classic image processing workflow” involving a limited number of classic image processing steps and algorithms that generated high-quality segmentations of these structures. These segmentations permitted initial analyses of basic morphometric features of these structures including size, number, shape, and location within the cell, and form the basis for more complicated feature parameterizations (**Fig. 1A**). To enhance the accuracy and robustness of these segmentations, we also developed a novel “iterative deep learning workflow” (**Fig. 1B**) that takes advantage of these high-quality classic segmentation results and applies them as an initial ground truth in an iterative deep learning-based approach to image segmentation.

These workflows are packaged into the Allen Cell Structure Segmenter, an open-source, Python-based toolkit for segmentation of 3D microscope images. We developed this toolkit to make both workflows accessible to cell biologists wishing to quantify and analyze their own image data. The Segmenter offers two key advantages over other image processing packages. First, the classic image segmentation workflow streamlines algorithm and parameter choice. Users are provided with a “lookup table” of classic image segmentation workflows for 20 intracellular structure localization patterns with varying morphological properties that can be used as a starting point for segmentation. Second, the iterative deep learning workflow provides users with tools to apply results from the classic segmentation workflow to generate ground truth segmentations for training deep learning models, without manual painting, and then to use these models to iteratively improve those segmentation results.

Results and Discussion

General overview of the Allen Cell Structure Segmenter

The goal of the Allen Cell Structure Segmenter is to make flexible, robust, state-of-the-art 3D segmentation methods accessible to cell biology researchers. While developed specifically for the 3D segmentation of intracellular structures, the Segmenter may also be applicable to a variety of other image segmentation applications. It seamlessly integrates a traditional image segmentation workflow and an iterative deep learning workflow to streamline the segmentation process (**Fig.1**). The classic image segmentation workflow is based on a restricted set of both standard and cutting-edge algorithms and tunable parameters (**Fig.1A**) that we identified to be optimal for segmenting over 30 different intracellular structure localization patterns. We created a suite of 20 intracellular structure segmentation workflows which we present in a lookup table as a starting point for users to solve their own segmentation tasks (**Fig. 2**). In the iterative deep learning workflow of the Segmenter, we describe two new strategies for preparing 3D ground truth images without laborious and subjective manual painting in 3D (**Fig. 1B**). The training and testing of the deep learning model are customized for intracellular structures in 3D fluorescence microscopy images and implemented as readable scripts for researchers without experience in deep learning.

The classic image segmentation and iterative deep learning workflows complement each other – the classic image segmentation workflow can generate sufficiently accurate segmentations for a wide range of intracellular structures for analysis purposes. However, when the accuracy or robustness of the optimal classic image segmentation workflow is insufficient, the iterative deep learning workflow can boost segmentation performance. Conversely, the classic segmentation workflow facilitates the application of deep learning models to 3D segmentation by generating candidate segmentations for an initial ground truth for model training. We have thus developed a new toolkit for 3D fluorescence microscopy image segmentation that (1) is applicable to a wide range of structures, (2) achieves state-of-the-art accuracy and robustness, and (3) is easy to use for cell biology researchers.

The classic image segmentation workflow

The challenge of designing classic image segmentation algorithms for a large number of distinct intracellular structures led us to a simple 3-step workflow. The steps include a restricted set of image processing algorithm choices and tunable parameters to effectively segment a wide range of structure localization patterns. The classic image segmentation workflow begins with a two-part pre-processing step, intensity normalization and smoothing, followed by the core segmentation algorithms, and ends with a post-processing step. Pre-processing prepares the original 3D microscope images for the core segmentation algorithms. Intensity normalization helps the segmentation be more robust to different imaging inconsistencies, including microscopy artifacts, debris from dead cells, etc., such that the same structures in different sets of images have similar intensity values above background when fed into the core segmentation algorithms (**Fig. 3A**). Smoothing reduces background noise from the microscope and other sources to improve segmentation algorithm performance. The choice of smoothing algorithm depends on the morphology of the intracellular structure (**Fig. 3B**). The core of the classic image segmentation workflow is a collection of algorithms for segmenting objects with different morphological characteristics (**Fig. 4**). This step takes in the pre-processed 3D image stack and generates a preliminary binary segmentation as input into the post-processing step. The final, post-processing step then fine-tunes the preliminary binary segmentations such as by filling holes or filtering by object size, turning them into

a final result (**Fig. 5**). The classic image segmentation workflow for a specific structure localization pattern may consist of just one of the core algorithms or it may require a combination of several core algorithms (**Fig. 2**).

Application of the classic image segmentation workflow to segmentation of over 30 intracellular structure localization patterns

We applied the classic image segmentation workflow to 3D images of over 30 fluorescently tagged proteins, each representing different intracellular structures. Structures were imaged in two different cell types, the undifferentiated hiPS cell and the hiPSC-derived cardiomyocyte. The tagged proteins representing these structures exhibited different expression levels and localization patterns in these two cell types. Certain structures also varied in their localization patterns in a cell cycle-dependent manner. Together, this led to over 30 distinct intracellular structure localization patterns, which we used to develop and test the classic image segmentation workflow. A key decision point for any segmentation task is the targeted level of accuracy. This is a function of several factors including: the size of the structure, the limits of resolution and detection for that structure, the goal of the subsequent analysis, and the effort required to obtain any given target accuracy. In general, we aimed to be consistent with observations in the literature about the structure and to obtain segmentations useful for 3D visualization. For example, our alpha tubulin segmentation workflow (**Fig. 2**) describes where the microtubules primarily localize and is detailed enough to generate a reasonable 3D visualization, but does not take known structural properties, such as the persistence length of microtubules, into account [Gan et al., 2016]. We also addressed the blurring of the boundaries of the structure arising from the resolution limits of fluorescence microscopy. Depending on both the contrast setting of the image and the parameters of a given segmentation algorithm, the resultant binary image can vary significantly. For example, segmentation of a mitochondrial tubule can result in segmented tubules of varying width (**Fig. 6**). To establish a consistent baseline of how to detect the blurred boundary, we used a fluorescently tagged mitochondrial matrix marker as a test structure and picked the segmentation parameter that most closely matches EM-based measurements of mitochondria in human stem cells ([Bukowiecki et al. 2014, Niclis et al. 2015]; see methods). We then used the resultant combination of contrast settings and object boundary setting as a consistent target for the creation of the other intracellular structure segmentation workflows.

Application of the classic segmentation workflow with these structure target criteria culminated in the intracellular structure look-up table of segmentation workflows for 20 selected distinct structure localization patterns (**Fig. 2**). These classic image segmentation workflows significantly improved segmentations compared with a set of 22 common baseline algorithms, including both global and local thresholding (**Fig. 7**). We found that for structures with similar morphological properties, the same series of algorithm choices resulted in successful segmentation (compare workflow diagrams in rows 5 and 6 in **Fig. 2**). However, the parameter values for the best result still varied. The structure segmentation look-up table and accompanying 3D z-stack movies (**Fig. 2** and allencell.org/segmenter) thus serve as a guide for which segmentation workflow (set of algorithm steps and parameter values) is a good starting point for a user's particular segmentation task. The classic image segmentation workflow component of the Allen Cell Structure Segmenter is openly accessible at allencell.org/segmenter. For each example in the lookup table, the specific workflow and accompanying algorithm parameters, fine-tuned on our data, are preset in a workflow-specific Jupyter notebook and accompanying "pseudocode" (see Supplemental Information) for rapid referencing and initial testing. If the preset parameters don't generate satisfactory segmentation results on user data, the parameters can be adjusted and assessed directly within the Jupyter notebook via an embedded 3D viewer. Step by step suggestions of which parameters to adjust are also included to help the user.

The iterative deep learning workflow

The aim of the iterative deep learning workflow (**Fig. 1B**) is to improve segmentation accuracy and robustness for situations where the classic image segmentation workflow is insufficient. It applies the concept of incremental learning [Schlimmer et al., 1986] to iteratively improve segmentation results. The segmentation results from the classic image segmentation workflow provide us with a set of 3D segmentation images that have the potential to be used as a ground truth for deep learning purposes. However, the accuracy of these results is often not uniform for all images. Instead, the greatest accuracy is generated in subsets of images or specific regions within images. We developed and tested two human-in-the-loop strategies, sorting and merging, to convert a set of classic image segmentation workflow results into an acceptable 3D ground truth image set for model training. These straightforward human-in-the-loop strategies do not involve any manual painting of the 3D structure, but still incorporate human knowledge into curating high-quality segmentation ground truth images. These first curated results from the classic image segmentation workflow can then be used as a starting point to train the first model. The segmentation results of the first model can once again be curated to provide a second, improved ground truth data set to create a second, improved segmentation model and so on for any number of iterations. Iterations can also be performed by combining segmentation results from several deep learning models via the merging and sorting strategies to further improve the resultant model. This approach thus eliminates the need for a large set of training data. The iterative deep learning workflow is implemented in an easily accessible way and with minimal tunable parameters. Specifically, users put raw images and training ground truths (segmentation images) in the same folder following a prescribed naming convention and set a few parameters that vary depending on image resolution and imaging modality. The details of building models, setting hyper-parameters, training the models, and so on, are handled automatically in a way that is designed and optimized for 3D fluorescence microscopy images.

Application of the iterative deep learning workflow generates a more accurate and robust lamin B1 segmentation

Image-to-image variation and cell-to-cell variation are two common scenarios in which the classic image segmentation workflow may not be sufficiently robust to data variation. For example, algorithms in the classic segmentation workflow do not always handle the image-to-image variation that arises within a dataset due to differences in biological and/or microscopy imaging conditions. In this case, a simple approach to preparing a ground truth segmentation image set is to sort segmented 3D images into “accept” or “reject” categories and only use the accepted images for initial model training (**Fig. 8**). The subsequent deep learning model may end up more robust to image-to-image variation because it incorporates contextual knowledge, which the classic segmentation workflow algorithms are incapable of doing. Similarly, within the same image, cells at different stages of the cell cycle may exhibit distinct structure morphologies or fluorescence intensities since interphase and mitotic structures can differ dramatically. In this case, two (or more) different segmentation parameters or algorithms might permit both types of structure localization patterns to be well-segmented, but two sets of parameters or algorithms cannot normally be applied to the same image. With the aid of a simple image editing tool, such as those available through ImageJ or ITK-SNAP, however, specific regions of interest within an image can be manually circled and masked. Different parameter sets or algorithms are then applied to each of these regions, and the results merged into one single segmentation ground truth for that image

(**Fig. 9**). A single deep learning model usually has sufficient representation capacity to learn all such variations within the image.

To demonstrate the segmentation accuracy and robustness achievable by the iterative deep learning workflow, we applied this workflow to the segmentation of lamin B1 images (**Fig. 10**). The lamin B1 localization pattern changes dramatically through the cell cycle, changing from a thin shell around the nucleus in interphase to a variable, wavy pattern during mitosis. This significant difference in localization patterns created a challenge for a classic image segmentation approach. To address this, we first built a classic image segmentation workflow to segment lamin B1 in interphase cells (**Fig. 2**). The best core algorithm to obtain accurate segmentation of this lamin B1 shell depended on generating an automatic seed in the center of each nucleus for the subsequent watershed algorithm. This automatic seeding was performed on the center slice of the 3D image stack, where most of the nuclei were easily detectable. However, this automatic seeding step sometimes failed, especially for cells with nuclei positioned above or below this center slice (blue arrows in **Fig. 10**). Further, as expected, mitotic cells in the image were not successfully segmented with this lamin B1 interphase-specific segmentation workflow (yellow arrows **Fig. 10**). From an initial set of 80 segmented images, only eight fell into the “keep” sorting category. The rest of the images either failed in the automatic seeding step or contained mitotic cells, which could therefore not be used as a ground truth. However, a first iteration deep learning model based only on these eight image stacks as its initial ground truth generated lamin B1 segmentations that picked up all interphase nuclei in all 80 images. This was an improvement from 85% to 100% when considering individual interphase nuclei and an improvement from 20% to 100% when considering entire image fields (e.g. an image field can fail if a single nucleus is not detected). In the second iteration of this workflow, we manually circled mitotic cells in 22 additional images and applied a separate classic image segmentation workflow for mitosis-specific lamin B1 localization patterns (**Fig. 2**). We then merged the interphase lamin B1 segmentation results from the first deep learning model with the mitotic lamin B1 segmentations obtained from the classic workflow to build a new training set out of these 22 images. This second iteration of a lamin B1 segmentation deep learning model generated successful lamin B1 segmentations for all interphase and mitotic cells in the original 80 images.

The Allen Cell Structure Segmenter is a powerful toolkit for the 3D segmentation of intracellular structures in fluorescence microscope images. The Segmenter combines a streamlined collection of selected standard and cutting-edge classic image segmentation algorithms with a suite of preset classic image segmentation workflows for 20 distinct intracellular structure patterns and with a novel iterative deep learning segmentation workflow. The classic image segmentation workflow together with the lookup table should provide users with a straightforward starting point for their own basic segmentation needs. More challenging segmentation tasks can benefit from the complementary approach of the classic and the iterative deep learning segmentation workflows. This combined approach permits training of deep learning models that can successfully segment different structure localization patterns within a single image. Two of the most significant challenges to creating robust useful segmentation methods for 3D quantitative analysis of cell behavior is to detect all instances of the cell or structure within the entire image and to do so successfully over time, especially if the cell or structure changes [Ulman et al., 2017]. This is required, for example, to capture the dynamic behavior of neighboring cells or neighboring structures within cells. The challenge here is that any cell or structure missed within one image or within one timepoint of a timeseries significantly reduces the analyzable data set. The success of our joint classic and iterative deep learning approach in improving the detection of all nuclei in an image from 20 to 100% with just one iteration of the model suggests great potential of applying this approach to the robust, automated segmentation of entire images of cells and intracellular structures in time.

Materials and Methods

Data collection for toolkit development

The image segmentation toolkit has been applied to data produced at the Allen Institute for Cell Science using gene-edited, human induced pluripotent stem cells (hiPSCs) in both the undifferentiated stem cell and hiPSC-derived cardiomyocytes. Briefly, CRISPR/Cas9 was used to introduce mEGFP and mTagRFP-T tags to proteins localizing to known intracellular structures [Roberts et al., 2017, Haupt et al., 2018]. Clonal, FP-tagged lines were generated for each intracellular structure of interest and were used in imaging experiments in which undifferentiated hiPS cells were labeled with membrane dye (CellMask Deep Red) and DNA dye (NucBlue Live) to mark cell boundaries and the nucleus (see the SOP at allencell.org). Edited hiPSC cell lines were differentiated into cardiomyocytes using a small-molecule protocol, as described previously (allencell.org and [Roberts et al., 2018]). For imaging, cells were plated onto glass bottom plates coated with matrigel for undifferentiated hiPS cells and polyethyleneimine and laminin for cardiomyocytes (see SOPs at allencell.org), respectively and were imaged using a ZEISS spinning-disk microscope with a 100x/1.25 Objective C-Apochromat W Corr M27, a CSU-X1 Yokogawa spinning-disk head or a 40x/1.2 NA W C-Apochromat Korr UV Vis IR objective, and Hamamatsu Orca Flash 4.0 camera. Imaging settings were optimized for Nyquist sampling. Voxel sizes were $0.108\text{ }\mu\text{m} \times 0.108\text{ }\mu\text{m} \times 0.290\text{ }\mu\text{m}$ in x, y, and z, respectively, for 100x, hiPSC images and $0.128\text{ }\mu\text{m} \times 0.128\text{ }\mu\text{m} \times 0.290\text{ }\mu\text{m}$ in x, y, and z, respectively, for 40x, cardiomyocyte images. The mEGFP-tagged Tom20 line was transfected with mCherry-Mito-7 construct (Michael Davidson, addgene #55102) using 6 μl per well of transfection mixture containing 25 μl Opti-MEM (ThermoFisher #31985-070), 1.5 μl GeneJuice (Millipore #70967) and 1 ug endotoxin free plasmid. Transfected cells were imaged the next day on a ZEISS spinning disk confocal microscope as above. All channels were acquired at each z-step.

Algorithms in the classic image segmentation workflow

Step 1: Pre-processing. To prepare images for segmentation, we first performed intensity normalization and smoothing. Our toolkit includes two normalization algorithms to choose from, min-max (MM) and auto-contrast normalization (AC). Min-max normalization transforms the full range of intensity values within the stack into the range [0,1]. Auto-contrast normalization adjusts the image contrast by suppressing extremely low/high intensities. To do this, the mean and standard deviation (std) of intensity is first estimated by fitting a Gaussian distribution to the whole stack intensity profile. Then, the full intensity range is cut off to the range [mean - a \times std, mean + b \times std], and then normalized to the range [0, 1] (**Fig. 3A**). The parameters, a and b, can be computed automatically based on a subset of typical images or can be user-defined. Auto-contrast is recommended by default. Min-max normalization should be used when the voxels with highest intensities are the target in the structure and should not be suppressed. For example, in “point-source” structures, such as centrin-2 (centrioles), the voxels with highest intensities usually reside in the center of the structure, making them critical to preserve. In addition to intensity normalization, there are three smoothing operations available in the pre-processing step: 3D Gaussian smoothing (G3), slice-by-slice 2D Gaussian smoothing (G2), and edge-preserving smoothing (ES; [Perona and Malik, 1990]). 3D Gaussian smoothing generally works well. However, if the target structure consists of dense filaments, an edge-preserving smoothing operation may be more effective (**Fig. 3B**). Slice-by-slice 2D Gaussian smoothing should be used when the movement of the intracellular structure is faster than the time interval between consecutive z-slices during live 3D imaging. In this situation, 3D smoothing may further aggravate the subtle shift of the structure in consecutive z-slices.

Step 2: Core segmentation algorithms. After pre-processing the images, they are segmented via a selection of core segmentation algorithms (**Fig. 1A**). 2D and 3D filament filters (F2 and F3; **Fig. 4A**; [Jerman et al., 2016]) are suitable for structures with curvi-linear shape in each 2D frame (e.g. Sec61 beta in **Fig. 4A**) or filamentous shape in 3D (e.g. alpha tubulin in **Fig. 4A**). The 2D and 3D spot filters (S2 and S3) compute the Laplacian of the Gaussian of the image in either 2D or 3D and thus can detect similar yet distinct spot-like localization patterns (**Fig. 4B**). The “point-source” desmoplakin localization pattern, exhibits as a round and fluorescence-filled shape in 3D. The S3 filter is more accurate for desmoplakin than the S2 filter, which stretches filled, round objects in the z-direction. For structures with a more general spotted appearance within each 2D frame instead of separate round structures (e.g. fibrillarin vs. desmoplakin in **Fig. 4B**), the S3 filter may fail to detect obvious structures while the S2 filter performs much better. The core watershed algorithm (W) can be used in two different ways. First, watershed can be applied to distance transformations of S3 filter results using local maxima as seeds to further separate proximal structures (**Fig. 4C**). Second, watershed can also be directly applied to the pre-processed image with seeds (detected by another algorithm) to segment structures enclosed in fluorescent shells (e.g. lamin B1 in **Fig. 4D**). The last core segmentation algorithm, masked object thresholding (MO) is designed for intracellular structure patterns with varying granularity or intensity (e.g. nucleophosmin in **Fig. 4E**). The MO threshold algorithm first applies an automated global threshold to generate a pre-segmentation result, which is used as a mask to permit an Otsu threshold to be applied within each pre-segmentation object. For example, the nucleophosmin localization pattern includes a primary localization to the granular component of the nucleolus and a weaker, secondary localization to other parts of both the nucleolus and nucleus. Therefore, we first apply a relatively low global threshold to roughly segment each nucleus. We next compute a local threshold within individual nuclei to segment the nucleophosmin pattern (**Fig. 4E**). Compared to traditional global thresholding, masked-object thresholding performs more robustly to variations in intensity of the nucleophosmin localization pattern in different nuclei within the same image.

Step 3: Post-processing. Three different algorithms are available for the final post-processing step in the workflow (**Fig. 5**). These algorithms refine the binary core segmentation algorithm result to return a final segmentation. Not all post-processing algorithms are needed for every structure. The first algorithm is a morphological hole-filling algorithm (HF) that can resolve incorrect holes that may have appeared in certain segmented objects to represent the target structure more accurately (**Fig. 5A**). Second, a straightforward size filter (S) can be used to remove unreasonably small or large objects from the core segmentation algorithm result. (**Fig. 5A**). Finally, a specialized topology-preserving thinning operation (TT) can be applied to refine the preliminary segmentation without changing the topology (e.g., breaking any continuous but thin structures). This thinning is accomplished by first skeletonizing the preliminary segmentation, then eroding the segmentation in 3D on all voxels that are not themselves within a certain distance from the skeleton (**Fig. 5B**).

Deep Learning Models and Training

The deep learning models employed in our iterative deep learning workflow are two fully convolutional networks specially customized for 3D fluorescence microscopy images: Net_basic and Net_zoom (**Fig. 11**; [Long et al., 2015] for more details about fully convolutional networks). Net_basic is a variant of a 3D U-Net [Çiçek et al., 2016] with (1) max pooling in all xyz dimensions replaced by max pooling in xy only, (2) zeros padding removed from all 3D convolution and (3) auxiliary loss added for deep supervision [Chen et al., 2016A]. Net_zoom has a similar architecture to Net_basic, but with an extra

pooling layer with variable ratio to further enlarge the effective receptive field. Such modifications are made to deal with anisotropic dimensions common in 3D microscopy images and to improve the performance in segmenting tenuous structures, such as the thin nuclear envelope.

In each training iteration, random data augmentation is applied on each image and a batch of sample patches are randomly cropped from the augmented images. In practice, the patch size (i.e., the size of model input) and batch size (i.e., the number of samples trained simultaneously in each iteration) depend on the available GPU memory. For example, a single Nvidia GeForce GPU with 12GB memory is used in our experiments. With this setup, we choose a batch size of 4 and each input sample patch has size $140 \times 140 \times 44$ voxels for Net_basic and $420 \times 420 \times 72$ voxels for Net_zoom. For data augmentation, we adopt a random rotation by θ (a random value from 0 to π) and a random horizontal flip with probability 0.5. Weighted cross-entropy is used in all the loss functions, where a per-voxel weight is taken as a separate input image (e.g., cost map). By default, we use a weight = 1 for all voxels, but one can assign a larger weight on those extremely critical regions or assign zeros to those regions that do not count for the loss function. Models are trained with Adam [Kingma and Ba, 2014] with constant learning rate 0.00001 and L2 regularization with weight 0.005.

Segmentation algorithm comparisons

Representative sample images from 20 structure localization patterns were used to compare segmentation results between the Allen Cell Structure Segmente classic image segmentation workflow, 14 global and 8 local thresholding algorithms (**Fig. 7**). All images corresponded to the maximum intensity projection of a z-slice of choice plus and minus one z-slice. Each image was segmented with 14 automatic global thresholding algorithms available in ImageJ under the Image/Adjust/Auto Threshold option and 8 local thresholding algorithms available in ImageJ under the Image/Adjust/Auto Local Threshold option. The local algorithms require an additional parameter that corresponds to the radius of the local domain over which the threshold will be computed. Radius values 8, 16, 32 and 64 were tested for each local thresholding algorithms. For each of these results, the segmentation algorithms that provided the segmentation most similar to the Allen Cell Structure Segmente result was identified based on the Dice Metric. Global threshold algorithms included Huang, Intermodes, IsoData, Li, MaxEntropy, Mean, Minimum, Moments, Otsu, Percentile, RenyiEntropy, Shanbhag, Triangle, Yen. Local threshold algorithms included Bernsen, Contrast, Mean, MidGrey, Niblack, Otsu, Phansalkar, Sauvola.

Determining mitochondrial width from published EM images

Methods: Mitochondrial widths were determined in human pluripotent stem cells and human embryonic stem cells using previously published EM images [Bukowiecki et al. 2014, Niclis et al. 2015], respectively. JPEG versions of the EM images obtained from the manuscripts were opened in Fiji and mitochondrial width was measured for 5-10 mitochondria per EM image. A line was manually drawn between the outer mitochondrial membranes along the smaller mitochondrial axis. Line lengths were measured and converted into nanometers using the original scale bars in the figures. Mitochondrial width was found to be 256 ± 22 nm for human pluripotent stem cells and 265 ± 34 nm for human embryonic stem cells (mean +/- 95% confidence interval). An average mitochondrial width of 260 nm was used in **Fig 6**.

Acknowledgements

We thank the entire Allen Institute for Cell Science team, who generated and characterized the gene-edited hiPS cell lines, developed image-based assays, recorded the high-replicate data sets suitable for image processing method development, and created the software infrastructure without whom this work would not have been possible. We especially thank the Allen Institute for Cell Science Gene Editing, Assay Development, Microscopy, and Pipeline teams for providing cell lines and images. We thank Winfried Wiegaebe, Derek Thirstrup, Rick Horwitz, Gaudenz Danuser, Wallace Marshall, Tom Misteli, Jennifer Lippincott-Schwartz, and the Allen Institute for Cell Science Assay Development team for many insightful discussions. We also thank Matt Bowden and Basudev Chauduri for technical support related to software package release. We thank the Gladstone Institute for providing initial wild-type stem cell lines. We thank the Allen Institute for Cell Science founder, Paul G. Allen, for his vision, encouragement, and support.

References

- [Arganda-Carreras et al., 2017] Arganda-Carreras, I., Kaynig, V., Rueden, C., Eliceiri, K. W., Schindelin, J., Cardona, A., and Sebastian Seung, H. (2017). Trainable weka segmentation: a machine learning tool for microscopy pixel classification. *Bioinformatics*, 33(15), 2424-2426.
- [Bukowiecki et al., 2014] Bukowiecki R., Adjaye J., and Prigione A. (2014). Mitochondrial function in pluripotent stem cells and cellular reprogramming. *Gerontology*, 60(2), 174-182.
- [Carpenter et al., 2006] Carpenter, A. E., Jones, T. R., Lamprecht, M. R., Clarke, C., Kang, I. H., Friman, O., Guertin, D. A., Chang, J. H., Lindquist, R. A., and Moffat, J., et al. (2006). Cellprofiler: image analysis software for identifying and quantifying cell phenotypes. *Genome Biology*, 7(10), R100.
- [Chen et al., 2016A] Chen, H., Qi, X., Cheng, J. Z., and Heng, P. A. (2016). Deep contextual networks for neuronal structure segmentation. In *AAAI Conference on Artificial Intelligence*, 1167-1173.
- [Chen et al., 2016B] Chen, J., Yang, L., Zhang, Y., Alber, M., and Chen, D. Z. (2016). Combining fully convolutional and recurrent neural networks for 3d biomedical image segmentation. In *Advances in Neural Information Processing Systems*, 3036-3044.
- [Chen et al., 2017] Chen, J., Banerjee, S., Grama, A., Scheirer, W. J., and Chen, D. Z. (2017). Neuron segmentation using deep complete bipartite networks. In *International Conference on Medical Image Computing and Computer-Assisted Intervention*, 21–29.
- [Çiçek et al., 2016] Çiçek, Ö., Abdulkadir, A., Lienkamp, S. S., Brox, T., and Ronneberger, O. (2016). 3D U-Net: learning dense volumetric segmentation from sparse annotation. In *International Conference on Medical Image Computing and Computer-Assisted Intervention*, 424-432.
- [De Chaumont et al., 2012] De Chaumont, F., Dallongeville, S., Chenouard, N., Hervé, N., Pop, S., Provoost, T., Meas-Yedid, V., Pankajakshan, P., Lecomte, T., Le Montagner, Y., et al. (2012). Icy: an open bioimage informatics platform for extended reproducible research. *Nature Methods*, 9(7), 690.
- [DRVISION, 2018] DRVISION. (2018). Aivia Cloud - AI Microscopy for Everyone. Retrieved November 8, 2018, from <https://www.drvtechnologies.com/aivia-cloud>.
- [Frangi et al., 1998] Frangi, A. F., Niessen, W. J., Vincken, K. L., and Viergever, M. A. (1998). Multiscale vessel enhancement filtering. In *International Conference on Medical Image Computing and Computer-Assisted Intervention*, 130–137.

[Gan et al., 2016] Gan, Z., Ding, L., Burckhardt, C. J., Lowery, J., Zaritsky, A., Sitterley, K., Mota, A., Costigliola, N., Starker, C. G., Voytas, D. F., Tytell, J., Goldman, R. D., and Danuser, G. (2016).

Vimentin intermediate filaments template microtubule networks to enhance persistence in cell polarity and directed migration. *Cell Systems*, 3(3), 252–263.

[Gibson et al., 2018] Gibson, E., Li, W., Sudre, C., Fidon, L., Shakir, D. I., Wang, G., Eaton-Rosen, Z., Gray, R., Doel, T., Hu, Y., Whyntie, T., Nachev, P., Modat, M., Barratt, D. C., Ourselin, S., Cardoso, M. J., and Vercauteren, T. (2018). NiftyNet: a deep-learning platform for medical imaging. *Computer Methods and Programs in Biomedicine*, 158, 113-122.

[Haupt et al., 2018] Haupt A., Grancharova T., Arakaki J., Fuqua M.A., Roberts B., and Gunawardane R.N. (2018). Endogenous protein tagging in human induced pluripotent stem cells using CRISPR/Cas9. *Journal of Visualized Experiments: JoVE*, 138.

[Hodneland et al., 2013] Hodneland, E., Kögel, T., Frei, D. M., Gerdes, H.-H., and Lundervold, A. (2013). CellSegm-a MATLAB toolbox for high-throughput 3d cell segmentation. *Source Code for Biology and Medicine*, 8(1), 16.

[Jerman et al., 2016] Jerman, T., Pernuš, F., Likar, B., and Špiclin, Ž. (2016). Enhancement of vascular structures in 3d and 2d angiographic images. *IEEE Transactions on Medical Imaging*, 35(9), 2107-2118.

[Kervrann et al., 2016] Kervrann, C., Sorzano, C. Ó. S., Acton, S. T., Olivo-Marin, J.-C., and Unser, M. (2016). A guided tour of selected image processing and analysis methods for fluorescence and electron microscopy. *IEEE Journal of Selected Topics in Signal Processing*, 10(1), 6-30.

[Kingma and Ba, 2014] Kingma, D. P. and Ba, J. (2014). Adam: A method for stochastic optimization. *arXiv preprint*, arXiv:1412.6980.

[Long et al., 2015] Long, J., Shelhamer, E., and Darrell, T. (2015). Fully convolutional networks for semantic segmentation. In *IEEE Conference on Computer Vision and Pattern Recognition*, 3431-3440.

[McQuin et al., 2018] McQuin, C., Goodman, A., Chernyshev, V., Kamentsky, L., Cimini, B. A., Karhohs, K. W., Doan, M., Ding, L., Rafelski, S. M., Thirstrup, D., et al. (2018). Cellprofiler 3.0: Next-generation image processing for biology. *PLoS Biology*, 16(7), e2005970.

[Neila et al., 2016] Neila, P. M., Baumela, L., González-Soriano, J., Rodríguez, J.-R., DeFelipe, J., and Merchán-Pérez, A. (2016). A fast method for the segmentation of synaptic junctions and mitochondria in serial electron microscopic images of the brain. *Neuroinformatics*, 14(2), 235-250.

[Niclis et al., 2015] Niclis, J.C., Murphy, S.V., Parkinson, D.Y., Zedan, A., Sathananthan, A.H., Cram, D.S., and Heraud, P. (2015). Three-dimensional imaging of human stem cells using soft X-ray tomography. *Journal of the Royal Society Interface*, 12(108), 20150252.

[Pawlowski et al., 2017] Pawlowski, N., Ktena, S. I., Lee, M. C., Kainz, B., Rueckert, D., Glocker, B., and Rajchl, M. (2017). Dltk: State of the art reference implementations for deep learning on medical images. *arXiv preprint*, arXiv:1711.06853.

[Perona and Malik, 1990] Perona, P. and Malik, J. (1990). Scale-space and edge detection using anisotropic diffusion. *IEEE Transactions on Pattern Analysis and Machine Intelligence*, 12(7), 629-639.

[Rafelski et al., 2012] Rafelski, S.M., Viana, M.P., Zhang, Y., Chan, Y.-H.M., Thorn, K.S., Yam, P., Fung, J.C., Li, H., Costa, L.d.F., and Marshall, W.F. (2012). Mitochondrial network size scaling in budding yeast. *Science*, 338(6108), 822–824.

[Robert et al., 2017] Roberts, B., Haupt, A., Tucker, A., Grancharova, T., Arakaki, J., Fuqua, M.A., Nelson, A., Hookway, C., Ludmann, S.A., Mueller, I.A. and Yang, R. (2017). Systematic gene tagging using CRISPR/Cas9 in human stem cells to illuminate cell organization. *Molecular Biology of the Cell*, 28(21), 2854-2874.

[Robert et al., 2018] Roberts, B., Arakaki, J., Gerbin, K.A., Malik, H., Nelson, A., Hendershott, M.C., Hookway, C., Ludmann, S.A., Mueller, I.A., Yang, R., and Rafelski, S.M. (2018). Scarless gene tagging of transcriptionally silent genes in hiPSCs to visualize cardiomyocyte sarcomeres in live cells. *bioRxiv*, 342881.

[Schindelin et al., 2012] Schindelin, J., Arganda-Carreras, I., Frise, E., Kaynig, V., Longair, M., Pietzsch, T., Preibisch, S., Rueden, C., Saalfeld, S., Schmid, B., et al. (2012). Fiji: an open-source platform for biological-image analysis. *Nature Methods*, 9(7), 676.

[Schlimmer et al., 1986] Schlimmer, J.C. and Fisher, D., (1986). A case study of incremental concept induction. In *AAAI Conference on Artificial Intelligence*, 86, 496-501.

[Smith and Barton, 2014] Smith, L. R. and Barton, E. R. (2014). Smash—semi-automatic muscle analysis using segmentation of histology: a matlab application. *Skeletal Muscle*, 4(1), 21.

[Sommer et al., 2011] Sommer, C., Straehle, C. N., Koethe, U., and Hamprecht, F. A. (2011). Ilastik: Interactive learning and segmentation toolkit. In *IEEE International Symposium on Biomedical Imaging: From Nano to Macro*, 2(5), 8.

[Ulman et al., 2017] Ulman, V., Maška, M., Magnusson, K.E., Ronneberger, O., Haubold, C., Harder, N., Matula, P., Matula, P., Svoboda, D., Radojevic, M., et al. (2017). An objective comparison of cell-tracking algorithms. *Nature Methods*, 14(12), 1141.

[Yushkevich et al., 2006] Yushkevich, P.A., Piven, J., Cody Hazlett, H., Gimpel Smith, R., Ho, S., Gee, J.C., and Gerig, G. (2006). User-guided 3D active contour segmentation of anatomical structures: Significantly improved efficiency and reliability. *Neuroimage*, 31(3), 1116–1128.

Figure Legends

Figure 1: Overview of the Allen Cell Structure Segmente. **(A)** The classic image segmentation workflow consists of three steps and includes a restricted set of image processing algorithm choices and tunable parameters. **(B)** The iterative deep learning workflow is used when the accuracy or robustness of the classic image segmentation workflow is insufficient. Two human-in-the-loop strategies, sorting and merging, can be iteratively applied to build 3D ground truth training sets from the classic image segmentation workflow results or resultant deep learning 3D segmentation models.

Figure 2: “Lookup table” of classic image segmentation workflows for 20 intracellular structure localization patterns. 18 of the 20 examples consist of image from one tagged protein representing the localization pattern. Examples in the bottom row are both lamin B1 images, but from interphase and mitotic stages of the cell cycle, each one representing a distinct localization pattern requiring a separate segmentation workflow. Each boxed region contains a pair of images with the original image on the left

and the result of the classic image segmentation workflow on the right. All original images presented here are single slices from a 3D z-stack of images available online (allencell.org/segmenter). Along the bottom of each image pair is a diagram outlining the steps for that segmentation workflow. The arrows within each diagram represent the transitions between the three steps (pre-processing, core segmentation, post-processing) of the classic image segmentation workflow (**Fig. 1**). Within each workflow step, two symbols directly adjacent to each other represent that the algorithms were applied sequentially while the symbol represents combining the results from both algorithms. The asterisk within the TT symbol for the sialyltransferase 1 workflow indicates that the topology-preserving thinning was only applied to the results from the masked object thresholding algorithm. The target result for LAMP-1 includes filling the larger lysosomes as the protein LAMP-1 labels the lysosomal membrane, but the target structure to detect is the entire lysosome.

Figure 3: Examples of available pre-processing algorithms in the Allen Cell Structure Segmenter. **(A)** Two different examples of non-muscle myosin IIB images with corresponding auto-contrast normalization (AC) results. **(B)** An example image of alpha tubulin demonstrating the difference between 3D Gaussian smoothing (G3) and edge-preserving smoothing (ES). The Otsu thresholding results of the original image and the images after two smoothing algorithms are shown to highlight the difference in detecting two parallel tubule bundles.

Figure 4: Examples of the available core segmentation algorithms in the Allen Cell Structure Segmenter. **(A)** Comparison between 2D and 3D filament filters (F2 and F3) applied to Sec61 beta and alpha tubulin images. The binary images are the results of applying a cutoff value (manually optimized for demonstration purpose) on the filter outputs. F2 performs better for curvi-linear shapes in each 2D slice, as seen in Sec61 beta images. F3 performs better for filamentous shapes in 3D, as seen in alpha tubulin images. Orange arrows indicate major segmentation errors. **(B)** Comparison between 2D and 3D spot filters applied to desmoplakin (left three panels) and fibrillarin (right three panels) images. Four consecutive z-slices are shown as four rows. The binary images are the results of applying a cutoff value (manually optimized for demonstration purpose) on the filter outputs. S3 performs better for round, fluorescence-filled shapes in 3D, as seen for desmoplakin images. In this case the S2 filter falsely detects desmoplakin in z-frames where the structure is already out of focus (orange arrows). S2 performs better for localization patterns with a general spotted appearance within each 2D frame, as seen in fibrillarin images. **(C)** Application of the watershed algorithm (W) on S3 segmentation of desmoplakin to separate merged spots. Left to right: The maximum intensity z-projection of the middle two z-slices of desmoplakin in **(B)** and the corresponding S3 result, the detected local maximum (small white dots) and the final results after applying the watershed (W) algorithm with the local maximum as seeds. **(D)** Application of the watershed algorithm (W) directly on pre-processed lamin B1 interphase images for segmentation with automatically detected seeds. The watershed line of the watershed output is taken as the segmentation result. **(E)** Application of the steps of masked object thresholding (MO) to nucleophosmin images. From left to right: an original image of nucleophosmin, the same image with adjusted contrast to highlight lower intensity signal throughout the nucleus, the result of a global threshold obtaining the overall shape of nuclei used as a mask, and the result of the Otsu threshold within individual nuclei as the final segmentation image. Compared to traditional global thresholding, masked-object thresholding is more robust to variations in intensity between different nuclei in the same image.

Figure 5: Examples of the available post-processing algorithms in the Allen Cell Structure Segmenter. **(A)** Demonstration of the hole-filling algorithm (HF) and the size filter (S) applied to the preliminary segmentation results of LAMP-1 images. The target result for LAMP-1 includes filling the larger lysosomes as the protein LAMP-1 labels the lysosomal membrane, but the target structure to detect is the entire lysosome. **(B)** Demonstration of the topology-preserving thinning algorithm (TT) on sialyltransferase 1 images. The magenta in the last column represents pixels that are removed after applying the TT algorithm.

Figure 6: Comparisons of detected object boundaries dependent on segmentation parameters. To identify a consistent target for detecting boundaries of the many different tagged intracellular structures, we demonstrate the effect of different segmentation parameters on the segmentation of mitochondrial tubules marked with a matrix-targeted mCherry in transiently transfected hiPS cells. The top row shows the same tubule with increasing brightness and contrast settings from left to right for visualization purposes only. The bottom row shows the result of increasing the kernel size parameter (S) while decreasing the threshold parameter (T) in the 2D filament filter segmentation algorithm, which was applied to this image. The brightness and contrast settings in the top row are set to match the segmentation results in the bottom row to demonstrate that each of the segmentation results are reasonable given the input image. The green line within the inset in the bottom row is 260 nm, the diameter of mitochondria based on EM images of human stem cells. The second column represents the segmentation result that the collection of classic image segmentation workflows in the look-up table aimed to consistently target for each intracellular structure localization pattern.

Figure 7: Comparison of segmentation results between the Allen Cell Structure Segmenter classic image segmentation workflow and 14 global and 8 local thresholding algorithms applied to the 20 structure localization patterns in the lookup table (**Fig. 2**). All images correspond to the maximum intensity projection of a z-slice of choice plus and minus one z-slice. The first column represents the original image. The second, third and fourth columns display the optimal global algorithm result, optimal local algorithm result, and the Allen Cell Structure Segmenter classic image segmentation workflow result, respectively (**Fig. 2**; see methods for list of algorithms tested).

Figure 8: Schematic of the human-in-the-loop sorting strategy for generating ground truth data sets from classic image segmentation workflow results for training subsequent 3D deep learning models. A classic image segmentation workflow was applied on a set of lamin B1 images, and then the segmented images were manually curated to sort out the images to keep. These images directly become the 3D deep learning training set.

Figure 9: Schematic of the human-in-the-loop merging strategy for generating ground truth data sets from classic image segmentation workflow results for training subsequent 3D deep learning models. Two different classic image segmentation workflows were applied to the same lamin B1 images. One workflow worked well on interphase lamin B1 localization patterns (yellow) and the other worked better on mitotic lamin B1 localization patterns (cyan). A mask made up of four circles with two different radii was manually created in Fiji with the “PaintBrush” tool. A single ground truth image was then merged

(⊗) based on the two segmentations by taking the segmentation displayed in yellow within the yellow area and the segmentation displayed in cyan within the cyan area on the mask. This merged ground truth image is used as part of the 3D deep learning training set.

Figure 10: Application of the iterative deep learning workflow to generate robust lamin B1 segmentations. The first two images in the top row represent a middle z-slice from the original lamin B1 image and a second version of the same image with adjusted contrast settings to highlight the fine structure in the lamin B1 mitotic localization pattern (yellow arrow). The third column in the top row represents the result of a standard Otsu thresholding segmentation as a baseline. The first image in the bottom row shows the Segmenter classic image segmentation workflow result. The middle image shows the result after the first iteration of the deep learning model trained by a ground truth set generated by sorting. Finally, the third image shows the result after the second iteration of the deep learning model trained on a ground truth set generated by merging. The blue arrow indicates an interphase lamin B1 localization pattern that was originally missing in the classic image segmentation workflow but was detected using the iterative deep learning models. The yellow arrow indicates a mitotic lamin B1 localization pattern that was detected after the second iteration of the deep learning model.

Figure 11: The architecture of the two deep neural networks used in the iterative deep learning workflow. The two networks, Net_basic and Net_zoom are almost identical in architecture. The layers and data flows that differ between Net_basic and Net_zoom are marked in purple and red, respectively. In general, the network consists of 7 core blocks connected by downsampling and upsampling layers. All core blocks have the same layers, detailed in the corner green box (two consecutive sets of 3D convolution with kernel size 3, batch normalization and ReLU activation). Both networks are attached to one main prediction branch and two auxiliary prediction branches. The main prediction block is one 3D convolution with kernel size 1, while auxiliary blocks have one 3D convolution with kernel size 3, followed by another 3D convolution with kernel size 1.

Figure 1

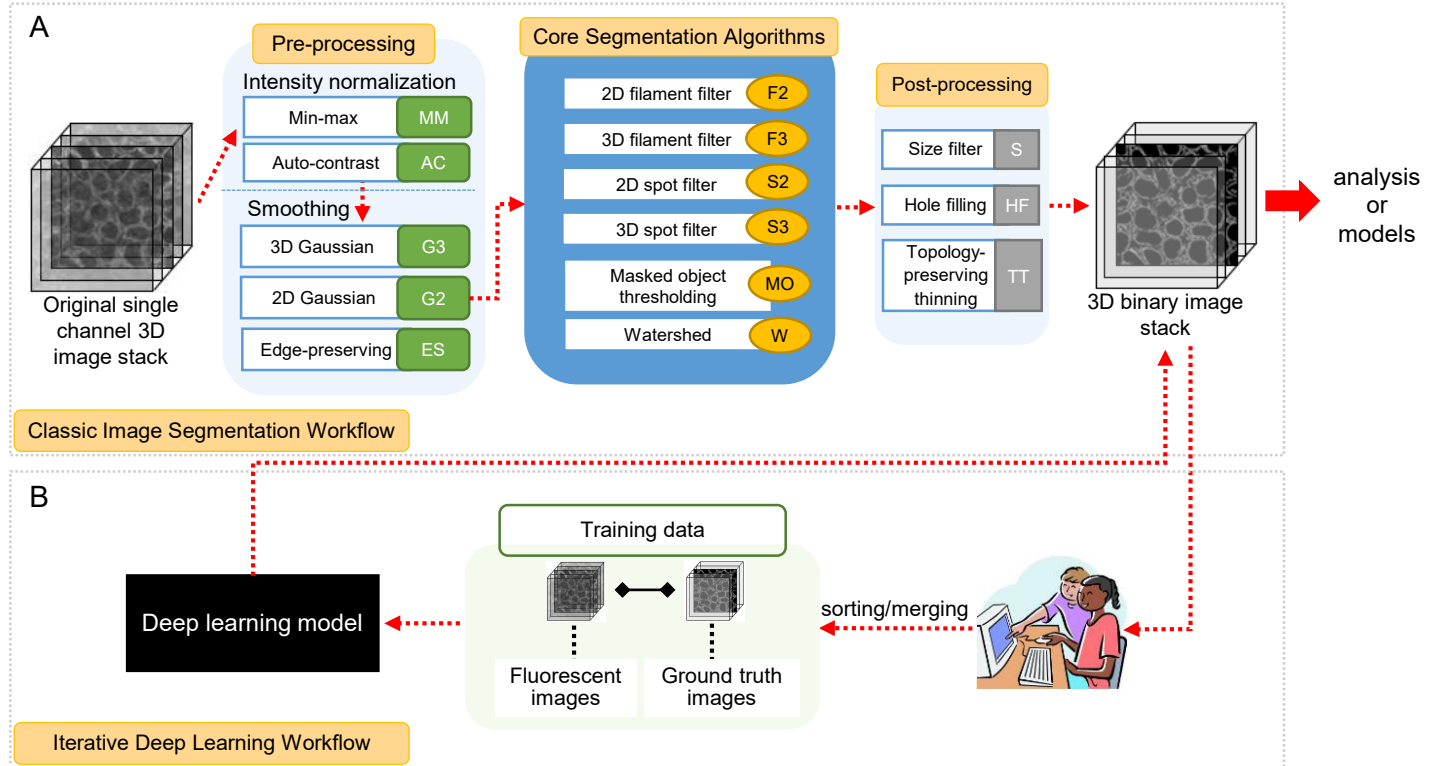
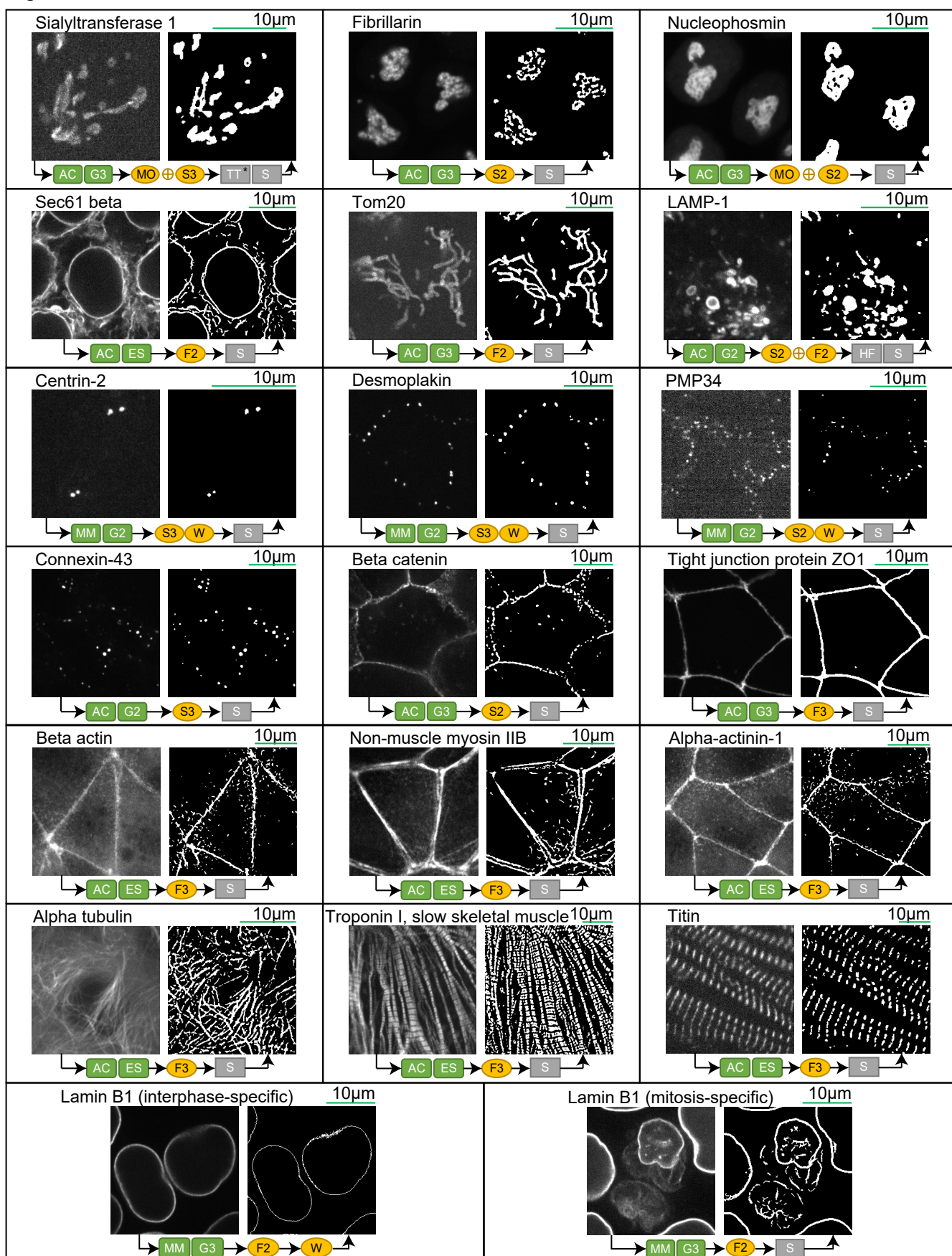


Figure 2



 Min-max normalization
 AC Auto-contrast normalization
 G2 2D Gaussian smoothing
 G3 3D Gaussian smoothing
 ES Edge-preserving smoothing

 F2 2D filament filter
 F3 3D filament filter
 S2 2D spot filter
 S3 3D spot filter
 MO Masked object thresholding

 W Watershed
 S Size filter
 HF Hole filling
 TT Topology-preserving thinning
^{*} TT only applied to MO

Figure 3

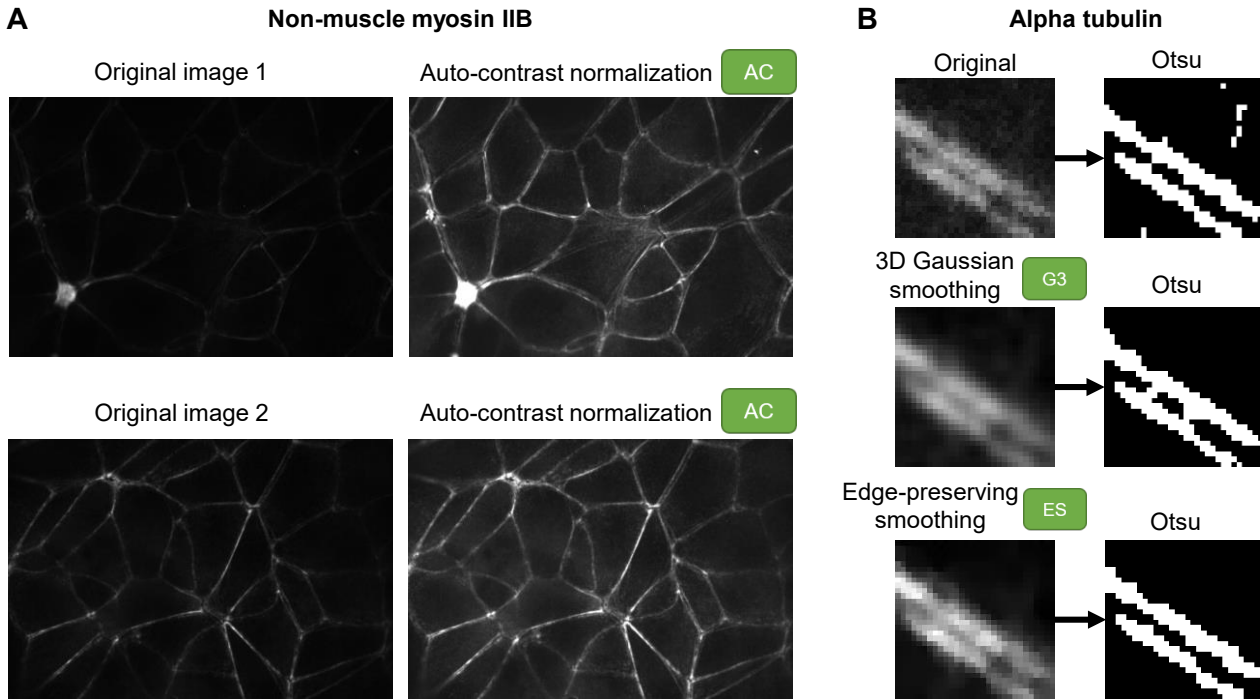


Figure 4

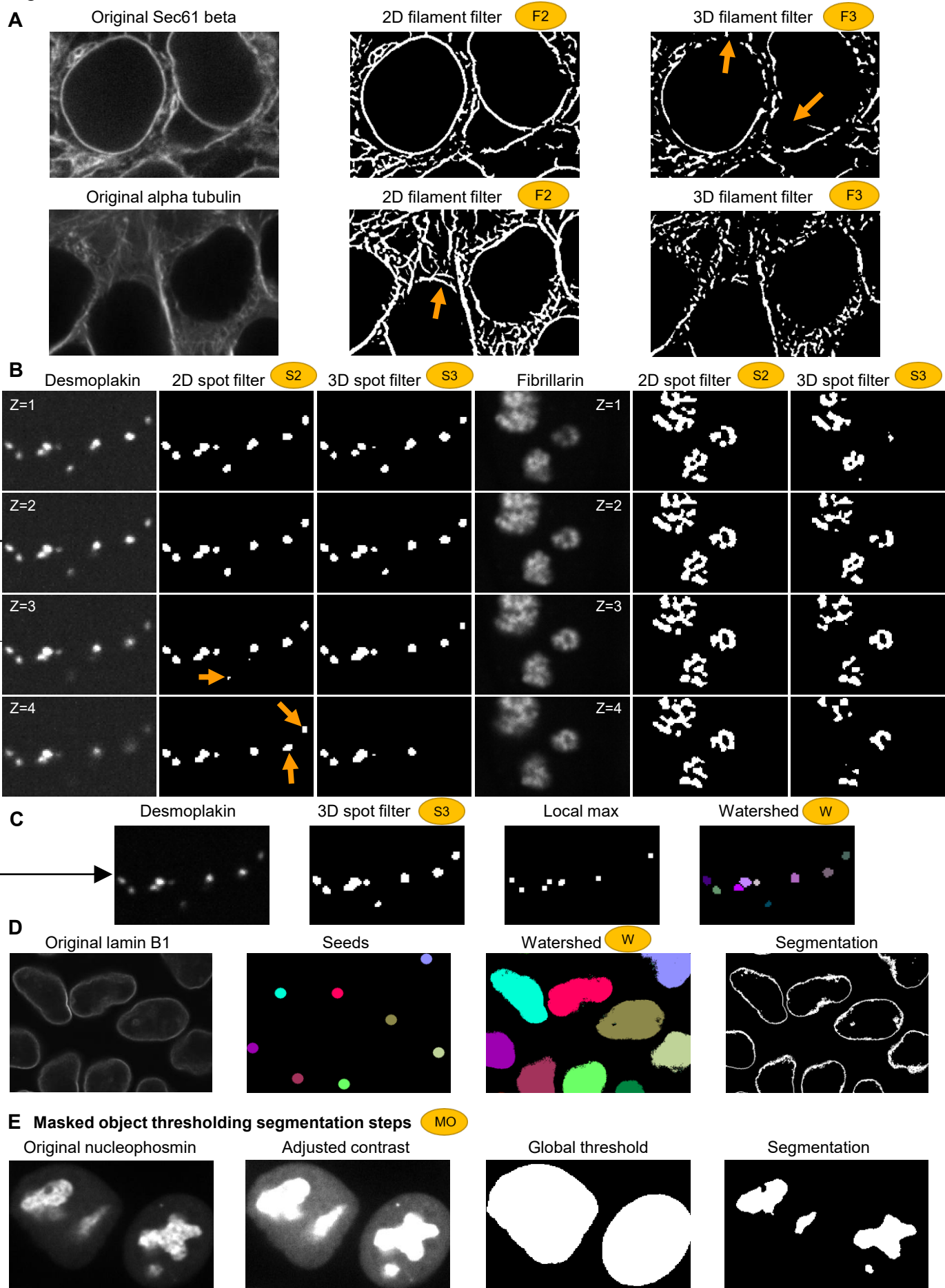


Figure 5

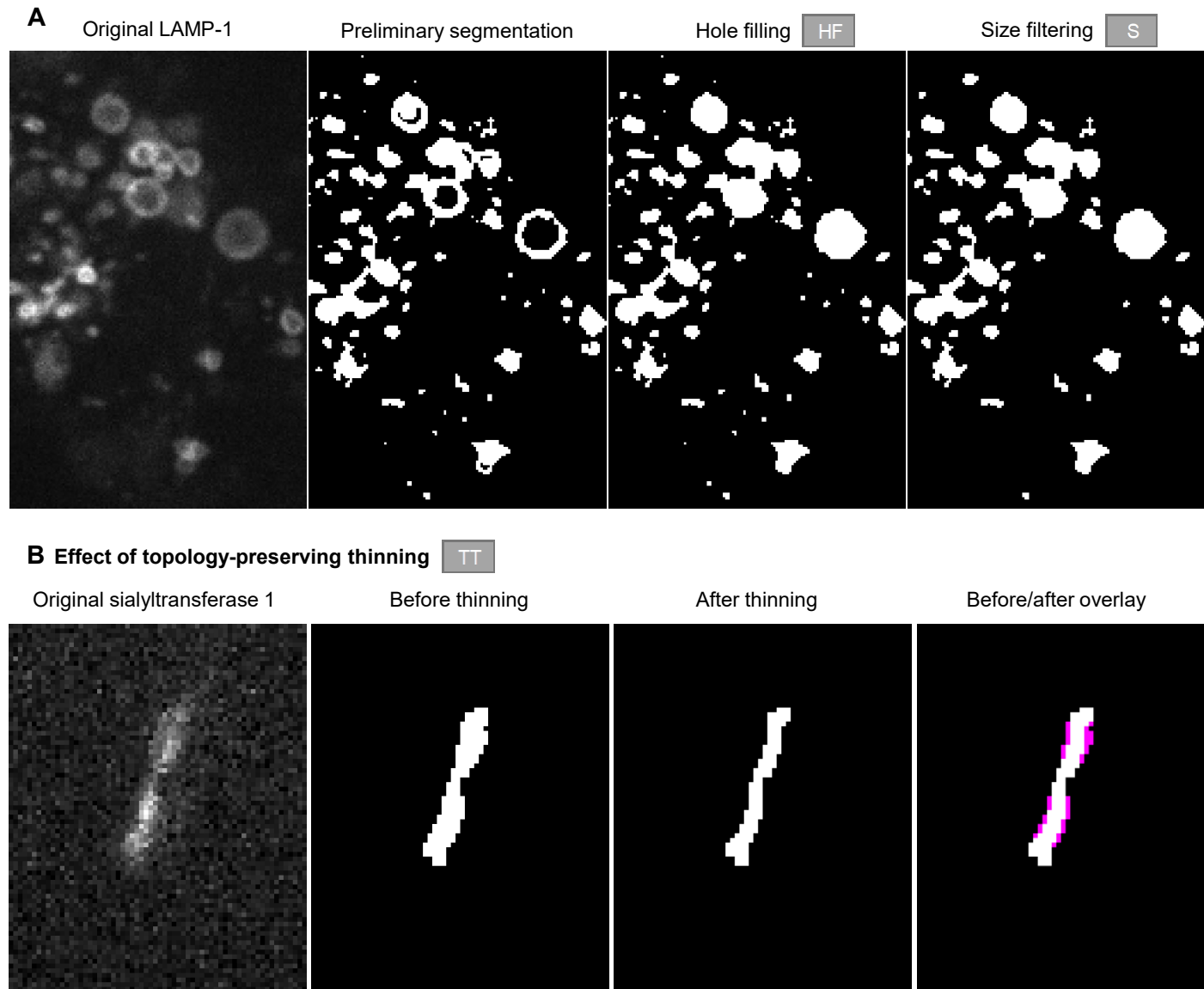


Figure 6

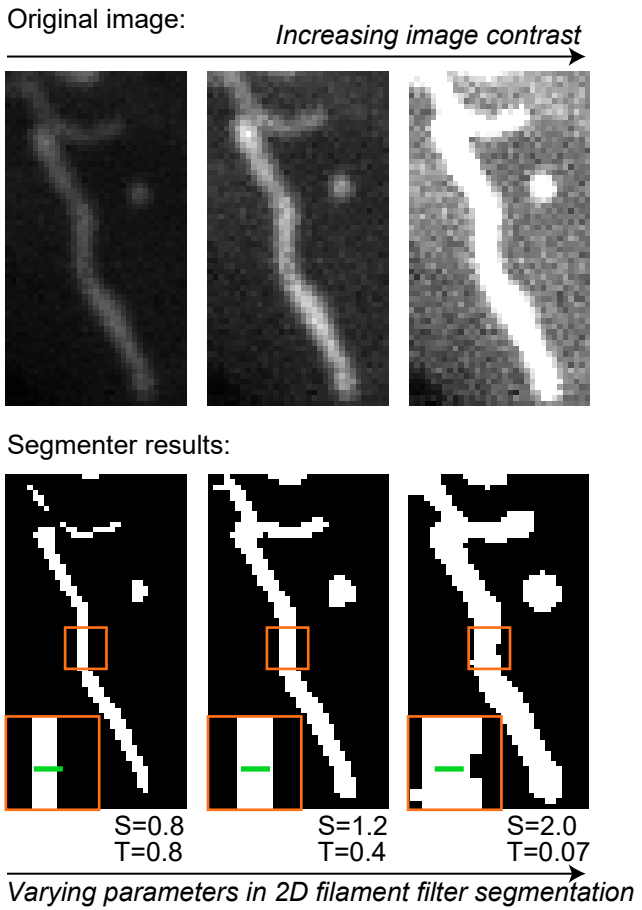


Figure 7

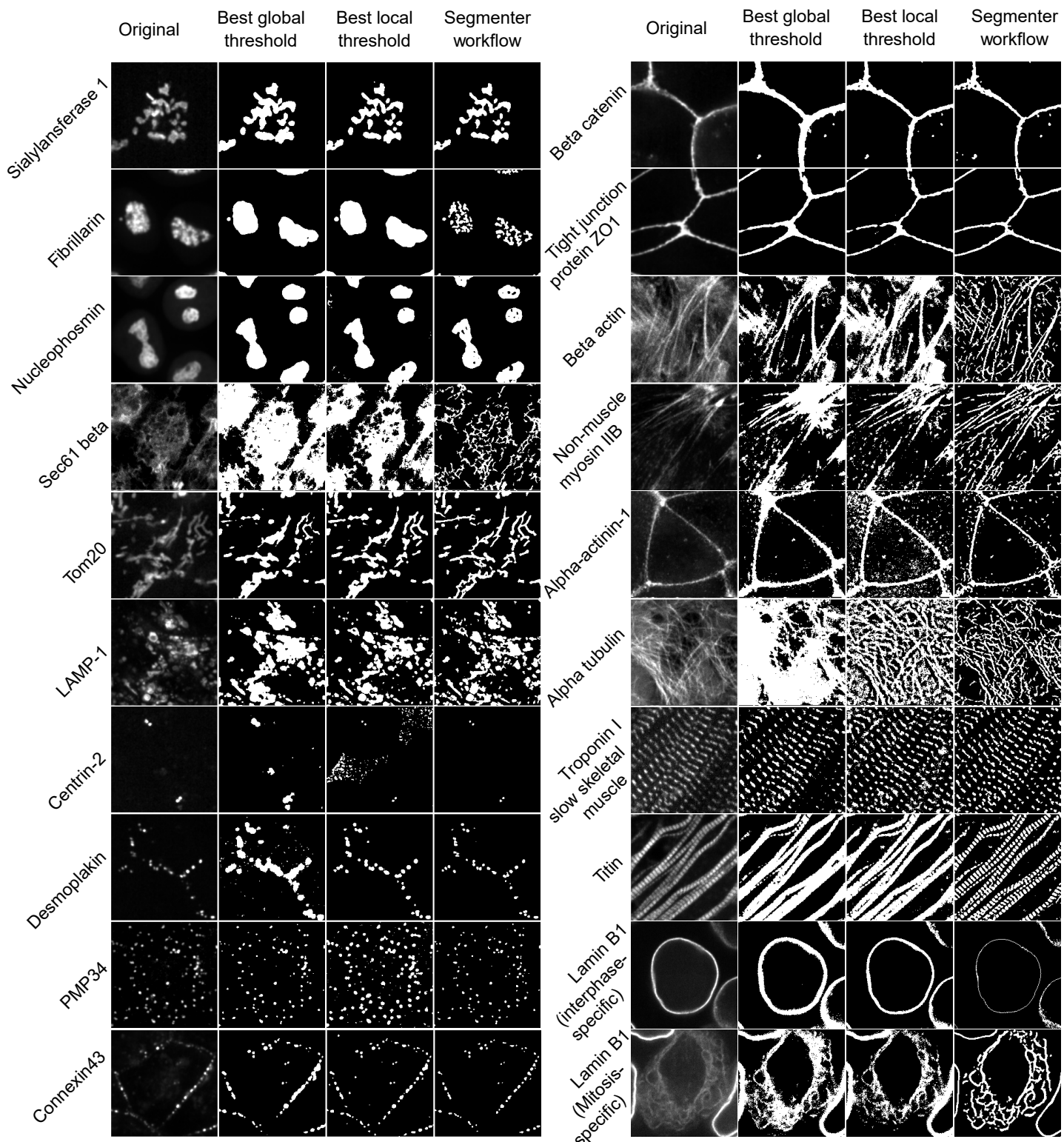


Figure 8

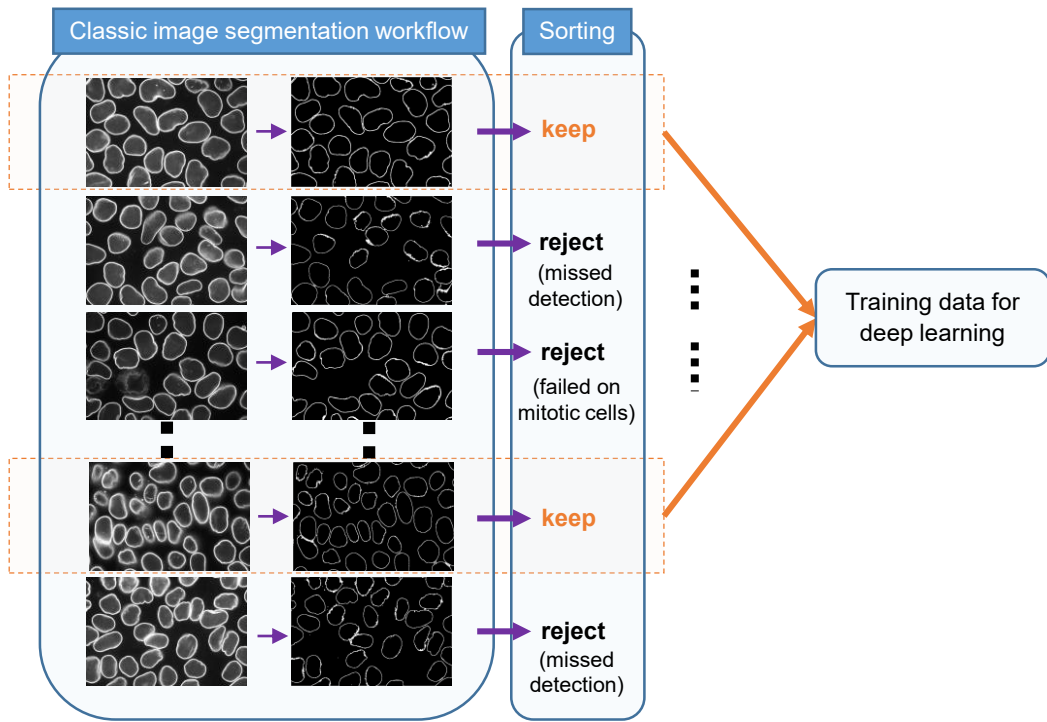


Figure 9

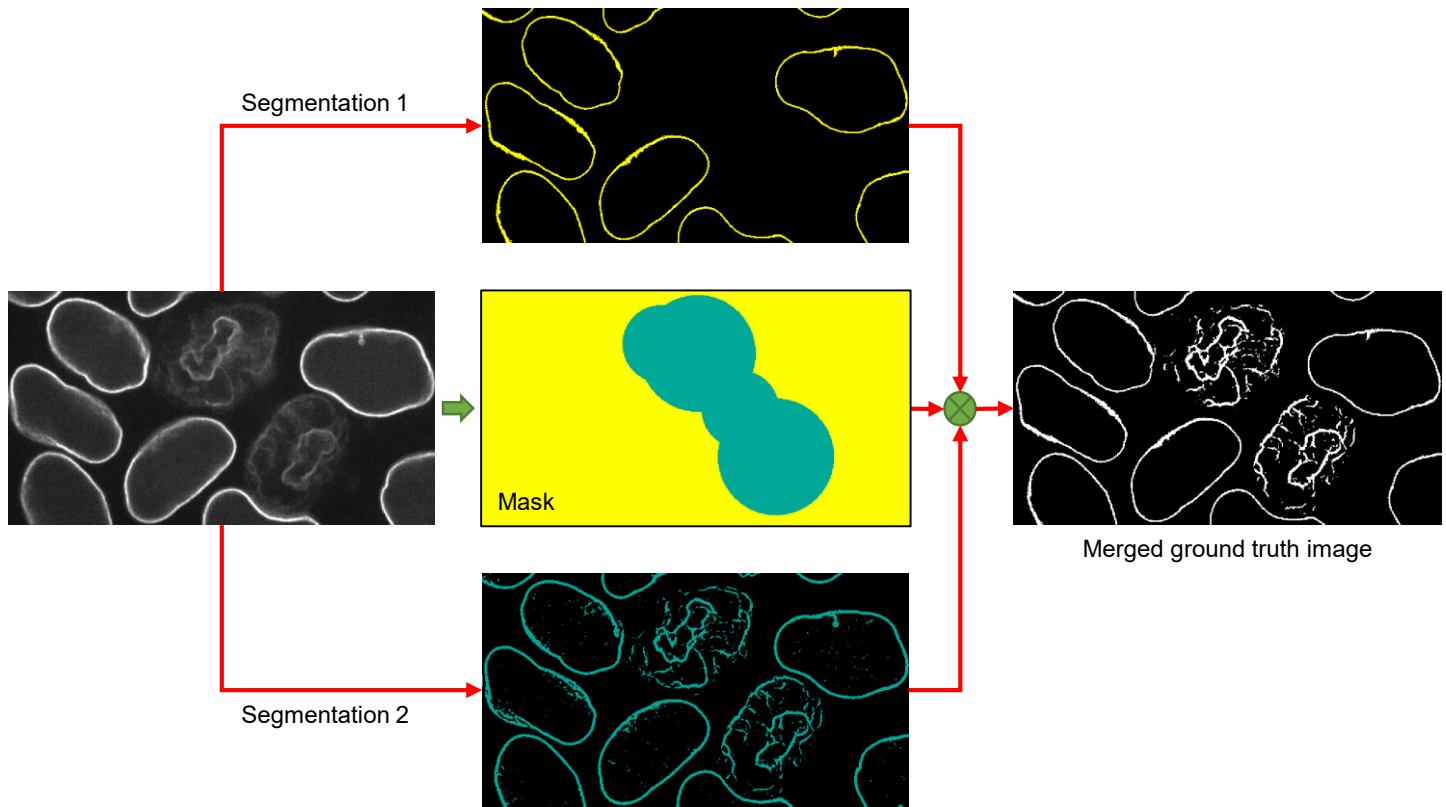


Figure 10

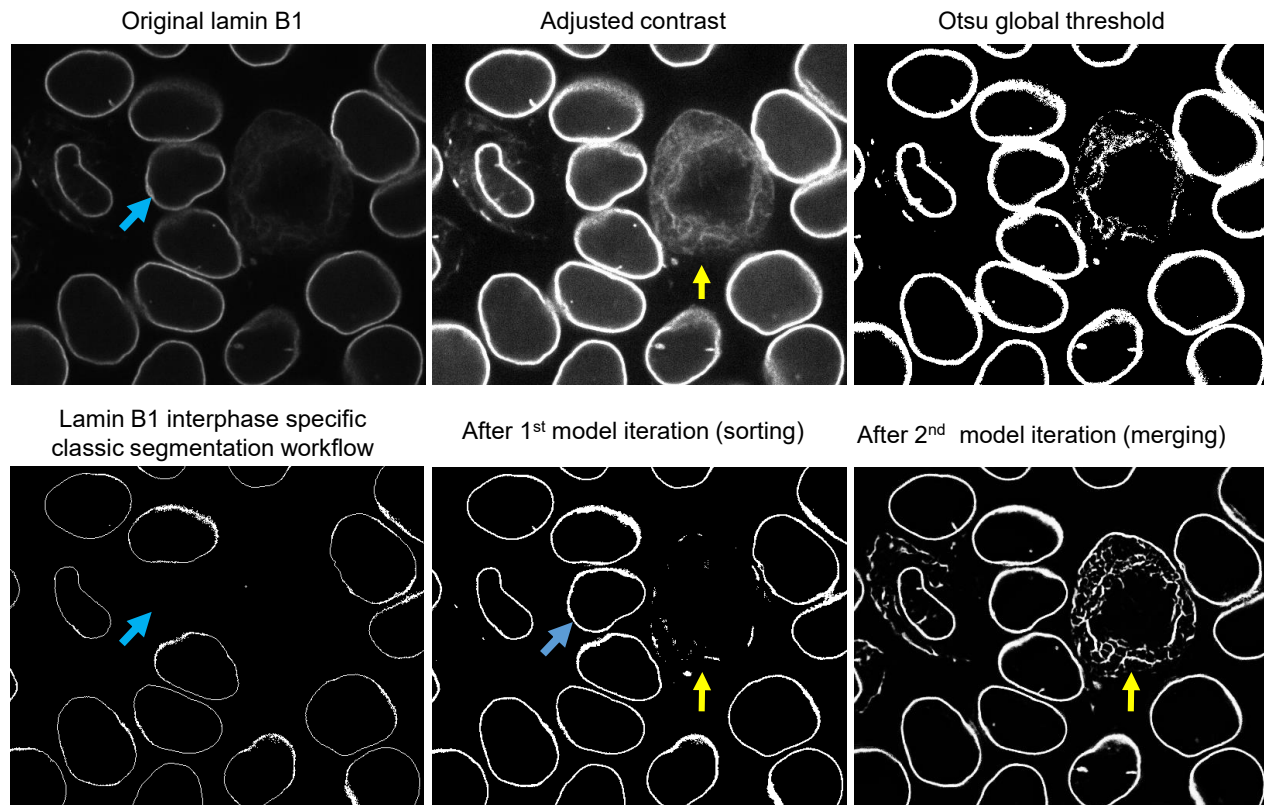


Figure 11

